The Astrophysical Journal, 829:125 (7pp), 2016 October 1 doi:10.3847/0004-637X/829/2/125

THE *XMM-NEWTON* AND *INTEGRAL* OBSERVATIONS OF THE SUPERGIANT FAST X-RAY TRANSIENT IGR J16328-4726*†

M. Fiocchi[1], A. Bazzano[1], L. Natalucci[1], P. Ubertini[1], V. Sguera[2], A. J. Bird[3], C. M. Boon [3], P. Persi[1], and L. Piro[1]
[1] INAF, Istituto di Astrofisica e Planetologia Spaziali, Via Fosso del Cavaliere 100, I-00133 Roma, Italy
[2] INAF, Istituto di Astrofisica Spaziale e Fisica Cosmica, Via Gobetti 101, I-40129 Bologna, Italy
[3] School of Physics and Astronomy, University of Southampton, University Road, Southampton, SO17 1BJ, UK
Received 2016 May 24; revised 2016 June 27; accepted 2016 July 4; published 2016 September 29

ABSTRACT

The accretion mechanism producing the short flares observed from the Supergiant Fast X-ray Transients (SFXT) is still highly debated and forms a major part in our attempts to place these X-ray binaries in the wider context of the High Mass X-ray Binaries. We report on a 216 ks *INTEGRAL* observation of the SFXT IGR J16328-4726 (2014 August 24–27) simultaneous with two fixed-time observations with *XMM-Newton* (33 and 20 ks) performed around the putative periastron passage, in order to investigate the accretion regime and the wind properties during this orbital phase. During these observations, the source has shown luminosity variations, from $\sim 4 \times 10^{34}$ to $\sim 10^{36}$ erg s^{-1}, linked to spectral properties changes. The soft X-ray continuum is well modeled by a power law with a photon index varying from ∼1.2 up to ∼1.7 and with high values of the column density in the range of ~ 2–4×10^{23} cm^{-2}. We report on the presence of iron lines at ∼6.8–7.1 keV, suggesting that the X-ray flux is produced by the accretion of matter from the companion wind characterized by density and temperature inhomogeneities.

Key words: binaries: general – X-rays: individual (IGR J16328-4726)

1. INTRODUCTION

IGR J16328-4726 was first reported as an unidentified transient source in the third *INTEGRAL* IBIS/ISGRI survey with a flux of 4 and 3.2 mCrab in the energy range 20–40 keV and 40–100 keV, respectively (Bird et al. 2007; Bodaghee et al. 2007).

The *Swift* XRT follow-up observations performed during a flare (on 2009 June 10) showed that the X-ray spectrum of the source was, at that time, well described by an absorbed power-law model with an $N_{\rm H} \simeq 8 \times 10^{22}$ cm^{-2} in excess of the expected Galactic value and a photon index $\Gamma \simeq 0.56$ (Grupe et al. 2009).

On the basis of its transient and recurrent nature, its short and intense flares and a dynamic range of $\sim 10^2$, this source has been classified as a candidate Supergiant Fast X-ray Transient (SFXT; Fiocchi et al. 2010). An orbital period corresponding to ∼10 days has been derived by Corbet et al. (2010) making use of *Swift*/BAT data. IGR J16328-4726 was observed by *XMM-Newton* on 2011 February 20 (corresponding to an orbital phase of ∼0.1) for a total exposure time of ∼22 ks (Bozzo et al. 2012). The analysis of these data showed a flux variation of a factor of ∼10 without significant variation of the spectral parameters ($N_{\rm H}$ and Γ). The average spectrum was well fitted with an absorbed power-law model with a column density of $\sim 17.5 \times 10^{22}$ cm^{-2}, a photon index of ∼1.5 and unabsorbed 2–10 keV flux of 1.7×10^{-11} erg cm^{-2} s^{-1}. The source was also within the field of view of *BeppoSAX* in 1998: the MECS X-ray data showed frequent microactivity typical of the intermediate state of SFXT and a weak flare with a duration of ∼4.6 ks (Fiocchi et al. 2013). During these observations, the photon index of the power-law model remained constant while the absorption column density was highly variable, spanning from ∼3 to $\sim 20 \times 10^{22}$ cm^{-2} across the transition from the low emission level ($F_{2-10\,\rm keV} \sim 3 \times 10^{-12}$ erg cm^{-2} s^{-1}) to the peak of the flare ($F_{2-10\,\rm keV} \sim 10^{-10}$ erg cm^{-2} s^{-1}). Romano et al. (2013) reported on the spectral analysis of a flare that occurred on 2009 June 10, and was observed with the *Swift*/XRT instrument. During the brightest X-ray emission (unabsorbed flux of 4.2×10^{-10} erg cm^{-2} s^{-1}) the photon index was ∼0.65 and the column density was $\sim 9 \times 10^{22}$ cm^{-2} in excess of the Galactic one. IR observations allowed confirmation of the nature of the companion as a O8I spectral-type star (Coleiro et al. 2013) and determined the source distance of 7.2 ± 0.3 kpc (Persi et al. 2015). At soft X-ray energies, long-term monitoring (2011–2013) with *Swift*/XRT allowed a detailed study of the emission outside the bright outbursts, identifying two low emission levels, both well described with a power-law model: the first has a photon index of ∼1.35 and a column density of $\sim 13.6 \times 10^{22}$ cm^{-2} at an observed flux of $F_{2-10\,\rm keV} \sim 16 \times 10^{-12}$ erg cm^{-2} s^{-1}, while the second one is fitted with a photon index of ∼0.3 and a column density of $\sim 1.5 \times 10^{22}$ cm^{-2} at an observed flux of $F_{2-10\,\rm keV} \sim 1.1 \times 10^{-12}$ erg cm^{-2} s^{-1}. These observations allowed an estimate of the lower limit of the dynamic range in this source of ∼750 (Romano et al. 2014).

This source has been reported as an SFXT characterized by an intermediate orbital period and a low flux variability in the review of Walter et al. (2015).

Outbursts from IGR J16328-4726 usually occur near the periastron passage, at a restricted phase range of its orbital period (10.068 ± 0.002 days, Fiocchi et al. 2013), allowing the use of fixed-time observations. In this paper, we report on the spectral results for two *XMM-Newton* (Jansen et al. 2001) observations, performed quasi-simultaneously with a long *INTEGRAL* (Winkler et al. 2003) observation performed at periastron (phase = 0.5).

* XMM Newton is an ESA science mission with instruments and contributions directly funded by ESA member States and the USA (NASA).

† INTEGRAL is an ESA project with instruments and science data center funded by ESA member states (especially the PI countries: Denmark, France, Germany, Italy, Switzerland, Spain), Czech Republic and Poland, and with the participation of Russia and the USA.

2. OBSERVATIONS AND DATA REDUCTION

The *INTEGRAL* observation commenced on 2014 August 24T11:38:42 (revolution 1448) and ended 2014 August 27T07:36:18 (revolution 1449). The *XMM-Newton* observations were performed on 2014 August 24T19:57:54 (UTC) for ∼33 ks (orbital phases ∼0.4) and on 2014 August 26T19:24:52 (UTC) for ∼20 ks (orbital phases ∼0.6).

The INTEGRAL/IBIS (Ubertini et al. 2003) data are processed using the Off-line Scientific Analysis (OSA v10.2) software released by the *INTEGRAL* Scientific Data Centre (Courvoisier et al. 2003).

Light curves and images of the source are extracted in the 23–50 keV energy band.

These runs were performed with the AVES cluster, designed to optimize performances and disk storage needed for the INTEGRAL data analysis by Federici et al. (2010).

XMM-Newton data were processed using version 14.0 of the Science Analysis Software (SAS). During both observations, EPIC MOS1 and PN operated in Full Frame Imaging mode and EPIC MOS2 in Partial Frame Imaging mode; the filter used was the medium thickness filter for both observations. Calibrated events are filtered using patterns 0–4 for the PN and 0–12 for both MOS. Extraction radii of 40″ were used for the source events for both the PN and MOS cameras. Background counts were extracted from source-free regions, in the same temporal intervals. Response and ancillary matrix files were generated using the SAS tasks RMFGEN and ARFGEN. All spectra were binned with a minimum of 20 counts per bin.

All spectral uncertainties and upper limits are given at 90% confidence for one parameter of interest.

3. ANALYSIS AND RESULTS

IGR J16328-4726 was not detected with IBIS in the entire observation (216 ks on-source) at a significance level greater than 4σ. The 3σ upper limit in the 23–50 keV energy range is $\sim 3 \times 10^{-10}$ erg cm^{-2} s^{-1}, corresponding to a luminosity of $L \sim 2 \times 10^{36}$ erg s^{-1}, using a distance of 7.2 kpc (Persi et al. 2015).

Due to the transient nature of IGR J16328-4726 we produced four mosaics (23–50 keV) with a shorter exposure time: for revolution 1448, we extracted one mosaic during the first ∼18 hr of observation ($T^1_{\rm start}$ = 56893.49 MJD), while for revolution 1449 we created three mosaics covering three periods of ∼13.3 hr each, with $T^2_{\rm start}$ = 56894.71 MJD, $T^3_{\rm start}$ = 56895.23 MJD, and $T^4_{\rm start}$ = 56895.74 MJD.

Intensities for each mosaic are reported in Figure 1 (triangles and upper limits) superimposed on the phase-folded light curve (from Figure 1 of Fiocchi et al. 2013). This plot shows increased activity around phase 0.5, most probably associated to the transit near periastron, though no strong flare was detected ($\leqslant 2 \times 10^{36}$ erg s^{-1}). Consequently, we noted that the source was significantly detected during phase 0.50–0.55 at 6.0 sigma with a flux corresponding to $\sim 3 \times 10^{-11}$ erg cm^{-2} s^{-1} ($L_X \sim 2 \times 10^{35}$ erg s^{-1}), while the first and last points of Figure 1 are 3σ upper limits. We summed the data in the period in which the source was detected, obtaining a spectrum with a net exposure time of ∼60 ks. With the *INTEGRAL* short observation, we are not able to constrain the physical spectral parameters and we report here the (23–50 keV) flux of $(2.8 \pm 1.2) \times 10^{-11}$ erg cm^{-2} s^{-1} with a photon index value fixed to 2.0 (χ^2/dof = 6.5/5). We note that IBIS data in phase ∼0.45–0.50 are not available because of the non-visibility period between one *INTEGRAL* revolution and the next. Unfortunately, the *XMM-Newton* observations were performed during two periods in which IGR J16328-4726 was not detected with IBIS, preventing a spectral study using simultaneous data.

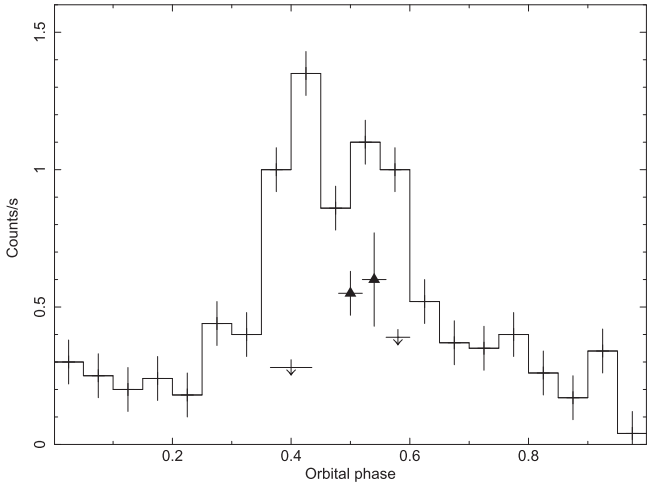

Figure 1. (23–50 keV) IBIS/ISGRI intensity of IGR J16328-4726 during revolutions 1448 and 1449 (triangles and upper limits) superimposed on the phase-folded light curve (crosses), constructed using the best orbital period determination of 10.068 days and a zero-phase ephemeris of MJD 52651.164 (from Fiocchi et al. 2013).

The EPIC PN background-subtracted light curves of IGR J16328-4726 in the 2–10 keV energy range are shown in Figure 2, at the ∼0.4 (left panel) and ∼0.6 (right panel) orbital phases.

Based on the spectral characteristics of this source, including the column density changes with the flux variations (Fiocchi et al. 2013), we performed a preliminary analysis for spectral variability by plotting the hardness versus total rates. We selected the energy bands 2–4 keV and 4–6 keV and computed the ratio $R = {\rm Rates}_{4-6\,{\rm keV}}/{\rm Rates}_{2-4\,{\rm keV}}$ and the sum $S = {\rm Rates}_{4-6\,{\rm keV}} + {\rm Rates}_{2-4\,{\rm keV}}$ of the count rates using a bin time of 240 s. These energy bands are chosen to investigate the possible column density and flux variations. We selected eight regions of interest from temporal intervals showing similar flux and similar hardness ratios. In Figures 3 and 4 (top panels), the total rate S (intensity) versus the ratio R (color) for the flares reported in Figure 2 are shown for both observations. Data from flares at similar flux levels and of similar hardness in the top panels of Figures 3 and 4 were combined to improve the statistical quality of the spectra and to better constrain the physical parameters. In particular, we consider the following regions in the plots of intensity versus color: a hard region with color $\geqslant$3.8, a soft region with color $\leqslant$3.8, a region with the intensity lower than ∼1 c s^{-1}, and a region with intensity higher than ∼1 c s^{-1}. Within these color-intensity regions, for the first *XMM-Newton* observation, we sum data from different flares when the points are superimposed on each others (*E*+*G*+*I* and *C*+*D*+*H*), while we consider single spectral states when the flare points are well separeted (A_1, A_2, *B*, and *F*). A similar criterion has been adopted for the second *XMM-Newton* observation, identifying two spectral states (*J*+*K*+*L* and *M*+*N*+*O*+*P*). The different intervals used for the time-selected spectroscopy were indicated with letters in Table 1 and in Figure 3 for the first *XMM-*

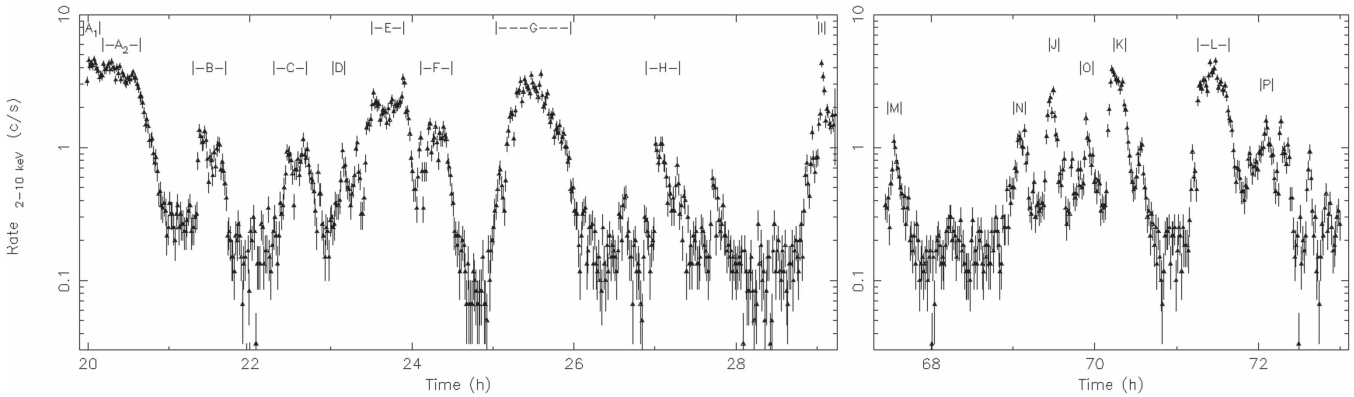

Figure 2. EPIC PN, background-subtracted light curves of IGR J16328-4726 in the 2–10 keV energy range. The bin size is 60 s and the time axis is in UTC hours from the start time of 56893 19:59:29.57 MJD. Letters indicate the time intervals used for selected spectral states (see the text for details). The left panel shows the first *XMM-Newton* observation at orbital phase ∼0.4 and the right panel shows the second *XMM-Newton* observation at orbital phase ∼0.6.

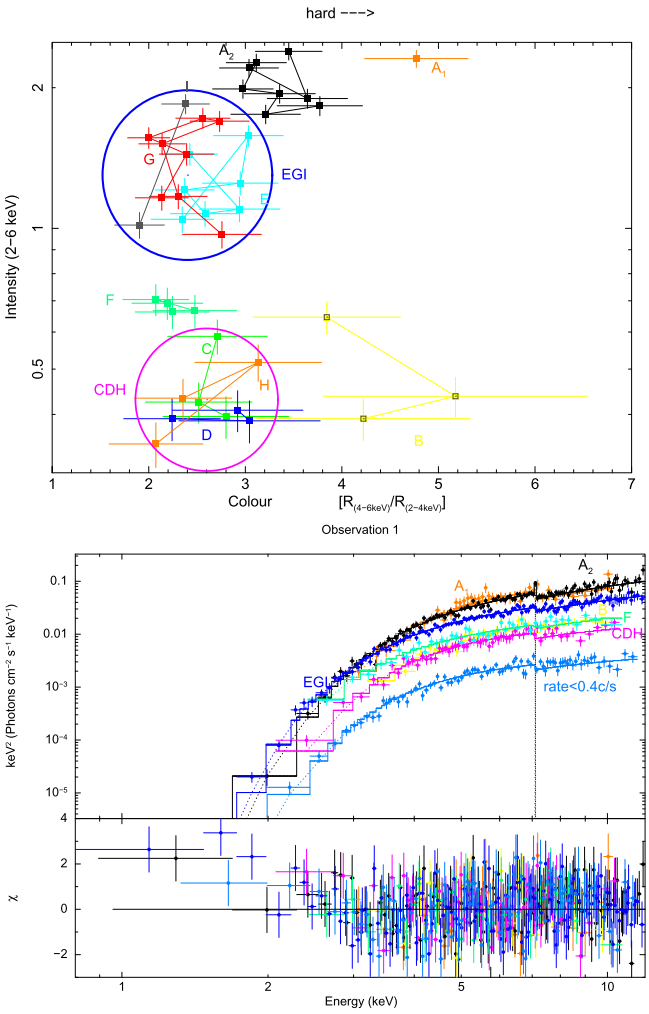

Figure 3. Top panel: hardness ratios $R = \mathrm{Rates}_{4-6\,\mathrm{keV}}/\mathrm{Rates}_{2-4\,\mathrm{keV}}$ for time intervals corresponding to flares displayed in Figure 2 plotted against the sum $S = \mathrm{Rates}_{4-6\,\mathrm{keV}}/\mathrm{Rates}_{2-4\,\mathrm{keV}}$ for the first observation. Large circles indicate the combined data from flares with similar flux levels and hardness. Bottom panel: unfolded spectra and the model in $E^2f\,(E)$ and residuals of the following spectral states: A_1 in orange, A_2 in black, EGI in blue, F in green, B in yellow, CDH in magenta, and the state with a rate lower than 0.4 c s^{-1} in light blue, fitted with the best model described in the text.

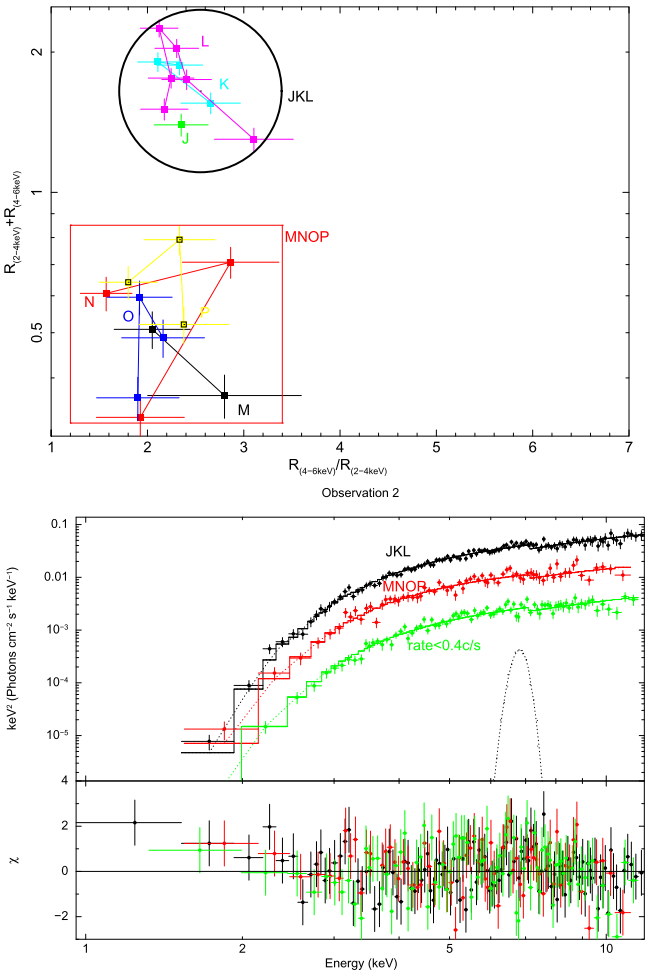

Figure 4. Top panel: hardness ratios $R = \mathrm{Rates}_{4-6\,\mathrm{keV}}/\mathrm{Rates}_{2-4\,\mathrm{keV}}$ for time intervals corresponding to flares displayed in Figure 2 plotted against the sum $S = \mathrm{Rates}_{4-6\,\mathrm{keV}}/\mathrm{Rates}_{2-4\,\mathrm{keV}}$ for the second observation. Large circle and square indicate the combined data from flares with the similar flux level and hardness. Bottom panel: unfolded spectra and the model in $E^2f\,(E)$ and residuals of the following spectral states: MNOP in red, JKL in black, and the state with a rate lower than 0.4 c s^{-1} in green, fitted with the best model described in the text.

Newton observation, and in Table 2 and in Figure 4 for the second *XMM-Newton* observation. In addition, spectra of the low emission level were obtained including events with count rates below 0.4 c s^{-1} (the bin time of the light curve is 60 s) corresponding to a net integration time of ∼15 ks and of ∼11 ks

Table 1
Results of the Time Selected Spectroscopy (Letters Mark the Same Time Intervals Displayed in Figure 2) During the First *XMM-Newton* Observation

Observation 1							
Parameter	*A1*	*A2*	*B*	*C+D+H*	*F*	*E+G+I*	<0.4 c s^{-1}
Start (MJD)	56893.832	56893.835	56893.890	56893.937 (*C*) 56893.968 (*D*) 56894.124 (*H*)	56894.007	56893.979 (*E*) 56894.049 (*G*) 56894.210 (*I*)	
Exp. PN[a]	0.2	1.7	0.6	1.9	0.9	3.6	14.6
Exp. MOS1[a]	0.2	1.9	0.7	2.1	0.9	4.0	16.3
Exp. MOS2[a]	0.2	1.9	0.7	2.1	0.9	3.9	16.0
$N_{\rm H}$	39^{+7}_{-6}	27 ± 2	30 ± 7	29 ± 3	19 ± 3	20.5 ± 0.9	26 ± 2
Γ	$1.8^{+0.4}_{-0.5}$	1.2 ± 0.1	1.2 ± 0.4	1.7 ± 0.2	1.2 ± 0.3	1.20 ± 0.08	1.7 ± 0.2
Unabs. Flux	208^{+53}_{-37}	140 ± 6	37^{+9}_{-7}	30^{+4}_{-3}	35 ± 4	73 ± 2	7.4 ± 0.5
E	...	7.1 ± 0.1	...	...	...	...	...
σ	...	<0.2	...	...	...	...	...
EW	...	40^{+15}_{-20}	...	...	...	...	...
χ^2/dof	...	261.8/232	...	...	...	...	...
χ^2/dof[b]	79.6/60	298.4/235	35.1/39	83.9/100	49.0/68	311.4/277	223.2/186

Notes. Γ is the power-law photon index. Unabsorbed Flux is in the 2–10 keV energy range in units of 10^{-12} erg cm^{-2} s^{-1} and $N_{\rm H}$ is in units of 10^{22} cm^{-2}. When a Gaussian component was added to the model, *E* is the centroid in keV, σ is the line width in units of keV, and EW is the equivalent width in eV.
[a] Exposure time in ks.
[b] χ^2/dof without the Gaussian component.

Table 2
Results of the Time Selected Spectroscopy (Letters Mark the Same Time Intervals Displayed in Figure 2) During the Second *XMM-Newton* Observation

Observation 2			
Parameter	*J+K+L*	*M+N+O+P*	<0.4 c s^{-1}
Start Time (IJD)	56895.892 (*J*) 56895.923 (*K*) 56895.967 (*L*)	56895.812 (*M*) 56895.873 (*N*) 56895.909 (*O*) 56895.998 (*P*)	
Exp. Time PN[a]	2.1	2.3	8.5
Exp. Time MOS1[a]	2.3	2.6	9.5
Exp. Time MOS2[a]	2.3	2.6	9.4
$N_{\rm H}$	20 ± 1	20 ± 2	21 ± 2
Γ	1.27 ± 0.09	1.4 ± 0.2	1.6 ± 0.2
Unabs. Flux	91 ± 4	27 ± 2	6.7 ± 0.6
E	6.8 ± 0.2	...	...
σ	<0.6	...	...
EW	148^{+100}_{-90}	...	...
χ^2/dof	216.7/242	...	...
χ^2/dof[b]	252.9/245	209.1/140	181.4/142

Notes. Γ is the power-law photon index. Unabsorbed flux is in the 2–10 keV energy range in units of 10^{-12} erg cm^{-2} s^{-1} and $N_{\rm H}$ is in units of 10^{22} cm^{-2}. A Gaussian component was added to the model, *E* is centroids in keV, σ is line width in units of keV, and EW is equivalent width in eV.
[a] Exposure time in ks.
[b] χ^2/dof without Gaussian component.

for the first and second *XMM-Newton* observations, respectively. The spectral analysis was performed for both EPIC MOS detectors and EPIC PN detector in the energy range 0.8–12.0 keV. We show only EPIC-PN spectra in the figures for clarity.

The PN and MOS spectra have been fitted simultaneously for each time interval using the model PHABS*POWERLAW in XSPEC with the interstellar abundances of Wilms et al. (2000).

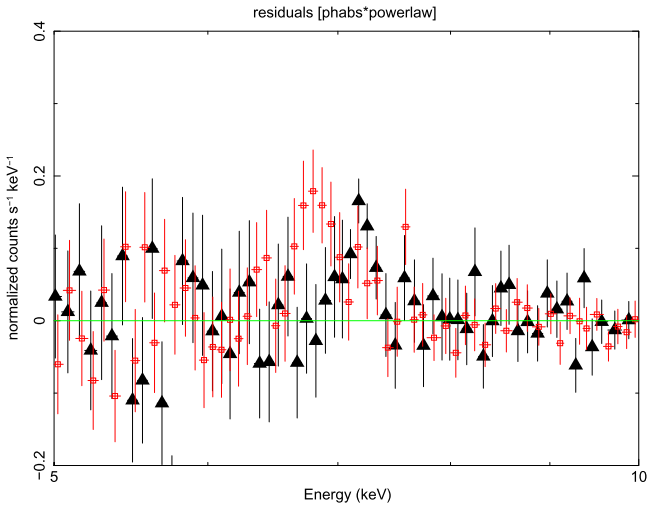

Figure 5. Residuals in units of count s^{-1} keV^{-1} of the A_2 (black triangles) and JKL (red squares) states, in the *XMM-Newton* first and second observations, respectively. The used model is an absorbed power law (see the text for details).

In the case of the spectral states named A_2 and JKL, the residuals show an evidence for a positive excess at iron line energies. For these spectral states, a Gaussian component was added to the power-law model. A zoom of residuals in the 5–10 keV band, using a simple absorbed power-law model, is shown in Figure 5 for the spectral states A_2 and JKL, from the first and second *XMM-Newton* observations, respectively. For each selected spectral state, the best-fit parameters are reported in Tables 1 and 2 for first and second observations, respectively.

Spectra and residuals with respect to the best model are shown in Figures 3 and 4 (bottom panels) for the first and second *XMM-Newton* observation, respectively.

For periods in which an emission line is significantly detected, we also report the χ^2 value obtained using a simple

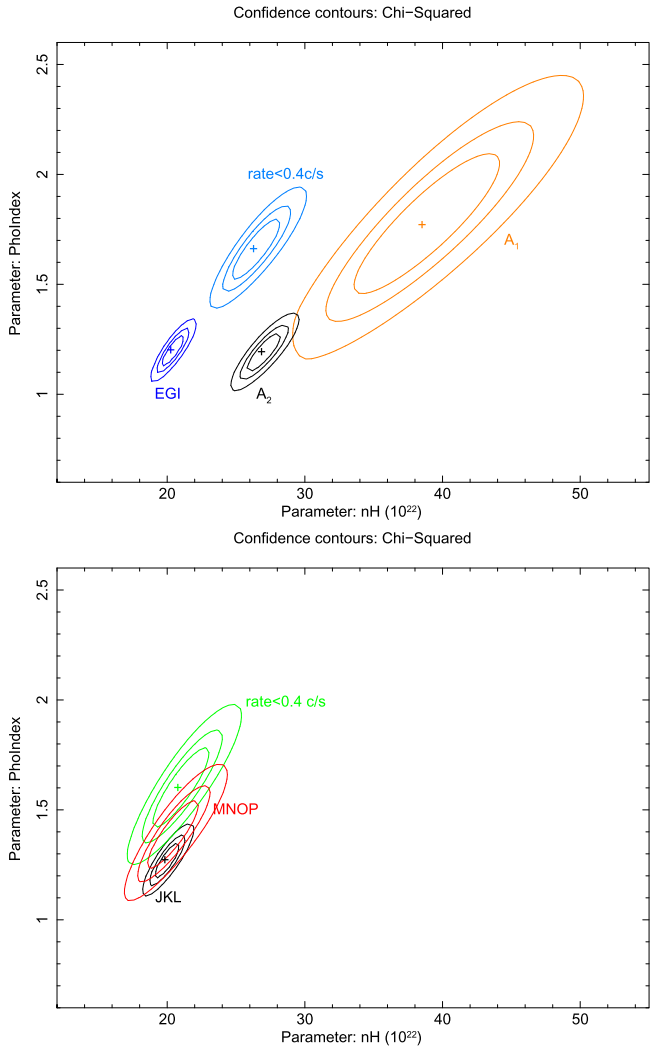

Figure 6. Top panel: confidence contours for the best-fit parameters to spectral states EGI, A_1, A_2, and the state with a rate lower than 0.4 c s^{-1}, for the first *XMM-Newton* observation. Bottom panel: confidence contours for the best-fit parameters to spectral states JKL, MNOP, and the state with a rate lower than 0.4 c s^{-1}, for the second *XMM-Newton* observation. For both observations, all contours are displaying the 68%, 90%, and 99% statistical confidence regions.

absorbed power law without a Gaussian component (see the last row of Tables 1 and 2).

In Figure 6 (top panel) the confidence contours (68%, 90%, and 99% confidence level) for the best-fit parameters to spectral states EGI, A_1, A_2 and "low state" are shown, for the first *XMM-Newton* observation. For clarity, we report on the better constrained contour plot only. In Figure 6 (bottom panel), we show the confidence contours for the best-fit parameters to spectral states JKL, MNOP, and the state with a rate lower than 0.4 c s^{-1}, for the second *XMM-Newton* observation.

During the first *XMM-Newton* observation, corresponding to the orbital phase ∼0.4, the source shows variations in both absorbing column density and photon index. The photon index of the states A_2 and EGI is ∼1.2 at fluxes of $\sim 10^{-10}$ erg s^{-1} cm^{-2} and it becomes ∼1.7 at flux of $\sim 7 \times 10^{-12}$ erg s^{-1} cm^{-2} ("low state"). The spectral parameters of states A_1 and B are not well constrained and are compatible with photon indices ranging from 1.1 to 2.5 (at a confidence level of 99%). The behavior of the photon index of the spectra A_2, EGI, and the low emission state follows the relation usually observed in accreting X-ray pulsars; X-ray emission is harder when the source is brighter. During the first *XMM-Newton* observation, there is evidence that the column density variation is independent of the unabsorbed flux as shown in Figure 6 (top panel), with different values at high fluxes (states EGI and A_2) and the same values at different fluxes (states A_2 and "low state"). During the second *XMM-Newton* observation, at orbital phase ∼0.6, both the photon index and the column density remain constant (see Figure 6 bottom panel).

4. DISCUSSION

The *XMM-Newton* observations have allowed us to perform an in-depth investigation of the transient source IGR J16328-4726 at two different orbital phases. We also followed the source variability in detail, revealing changes in its spectral shape. The photon index shows significant variations, with values ranging from ∼1.2 during high flux intervals (states EGI and A_2) to ∼1.7 during a low state (see Table 1 and Figure 6, top panel) in the first *XMM-Newton* observation (at an orbital phase of 0.4). This spectral softening at low luminosity is in agreement with the standard behavior observed in SFXTs. Indeed, X-ray spectra during very strong flares are usually well described by a flat power law ($\Gamma \sim 0$–1), while the photon index increases to values of $\Gamma \sim 1$–2 at lower luminosities of $\sim 10^{33-34}$ erg s^{-1} (see Romano et al. 2011, 2014; Sidoli 2011). Changes to the photon index corresponding to changing luminosity are not observed during the second *XMM-Newton* observation at orbital phase ∼0.6.

In Figure 7, we show the spectral index (top panel) and the column densities (bottom panel) against unabsorbed fluxes in the 2–10 keV energy range, using spectral analysis of time-selected states reported in Tables 1 and 2 and archival results. In this way, we can track the unabsorbed flux variations by two orders of magnitude. We show parameter values for the first *XMM-Newton* observation in black points, for the second *XMM-Newton* observation in red, for the *BeppoSAX* data in green (from Fiocchi et al. 2013), for the *Swift* XRT data in blue (from Romano et al. 2013), and *XMM-Newton* data from Bozzo et al. (2012) in magenta. Since these data all cover similar energy ranges, the derived $N_{\rm H}$ values should be comparable. Squares with circles indicate spectral parameters measured during average low emission levels, squares alone indicate parameters measured during an active period.

The analysis of different flux states confirms changes in the column density, previously observed using *BeppoSAX* data (Fiocchi et al. 2013) and highlights the variation of spectral index: from the top panel of Figure 7 it is clear that the photon index shows significant variations without any clear correlation with unabsorbed flux. The bottom panel of Figure 7 shows that the $N_{\rm H}$ values at flux lower than $\sim 10^{-11}$ erg s^{-1} cm^{-2} and greater than $\sim 4 \times 10^{-10}$ erg s^{-1} cm^{-2} do not confirm the linear correlation between flux and column density observed in this object in the past (Fiocchi et al. 2013), when we consider two orders of magnitude in flux. In a restricted range of fluxes, from $\sim 10^{-11}$ to $\sim 2 \times 10^{-10}$ erg s^{-1} cm^{-2} this correlation still persists.

To investigate the possible column absorption and the orbital phase correlation, we report in Figure 8 the column density against the orbital phase. We display column density values according to colors in Figure 7. Squares with circles indicate spectral parameters measured during average low emission

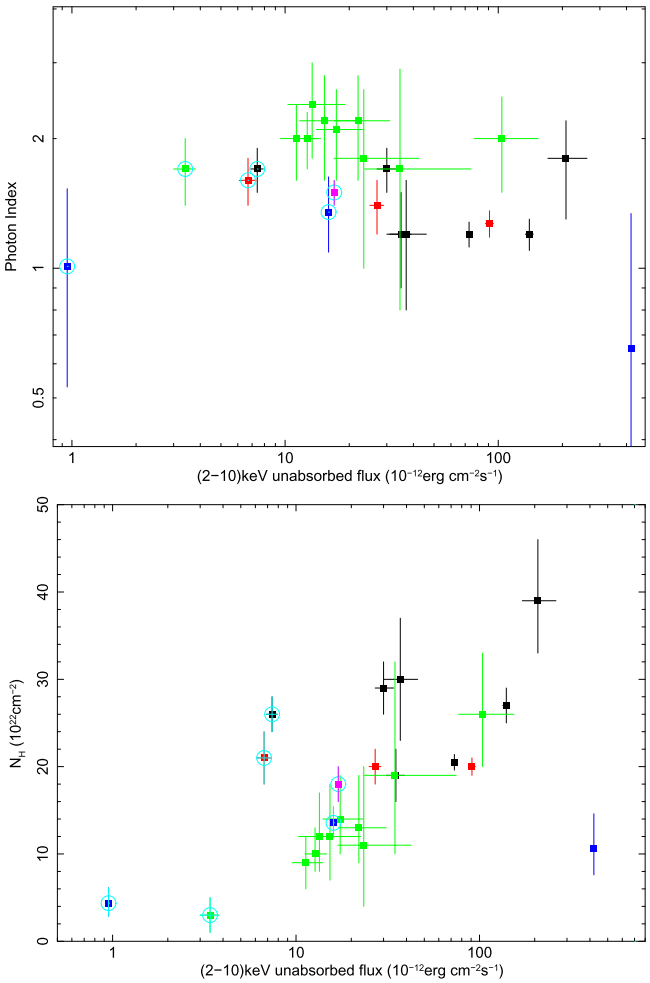

Figure 7. Top panel: photon index against unabsorbed fluxes in units of 10^{-12} erg cm^{-2} s^{-1} in the 2–10 keV energy range. Bottom panel: column density in units of 10^{22} cm^{-2} plotted vs. unabsorbed flux in units of 10^{-12} erg cm^{-2} s^{-1} in the 2–10 keV energy range. To do this comparison, the values from previous observations were computed with the same interstellar abundances used in this paper (Wilms et al. 2000). For blue squares (*Swift* data from Romano et al. 2013, 2014) the flux uncertainties are not available. For details on the colors, see the text.

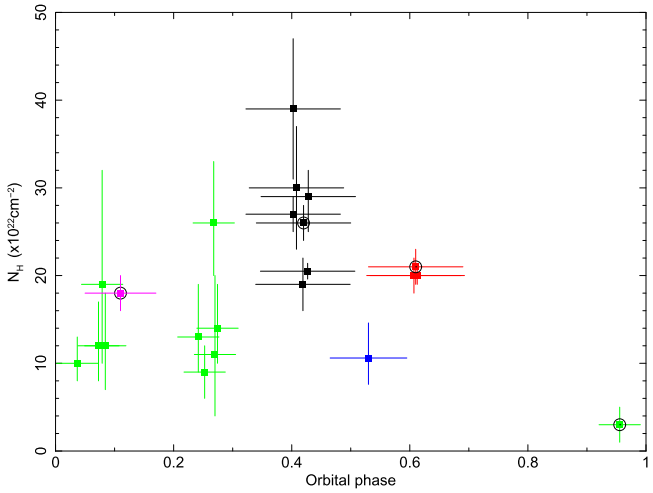

Figure 8. Column density in units of 10^{22} cm^{-2} plotted vs. orbital phase. We display column density values for the first *XMM-Newton* observation in black, the second *XMM-Newton* observation in red, the *BeppoSAX* in green (from Fiocchi et al. 2013), *Swift* XRT in blue (from Romano et al. 2013), and *XMM-Newton* in magenta (from Bozzo et al. 2012). Squares with circles indicate spectral parameters measured during average low emission levels, squares alone indicate parameters measured during an active period.

levels, squares alone indicate parameters measured during an active period. Spectral parameter values obtained from spectra with long exposure times (covering approximately one phase) are not included in this plot.

Figure 8 shows that there are significantly higher values of the column density during the active time interval corresponding to the orbital phase of 0.4. We note that the average low emission level (squares with circles in Figure 8) shows a maximum at phase ∼0.4 and a minimum at phase ∼0.95. These data show that there could be two levels of the density variations: the first corrisponding to the average low emission states and the second considering the active periods. During the low emission levels (circles of Figure 8), the $N_{\rm H}$ follows the same behavior that the IBIS intensity (23–50 keV) has versus the orbital phase, with a maximum value at phase ∼0.5 and lower values at phases ∼0.1 and ∼1.0. During the active periods, the $N_{\rm H}$ variations are not correlated with the orbital phase and could indicate changes in the accreting material on the neutron star. Obtained $N_{\rm H}$ values rule out that the observed low emission level (flux lower than $\sim 10^{-11}$ erg s^{-1} cm^{-2}) can be due to obscuration of the emitting region by circumstellar material, because there are in fact values of the column density during the low emission level that are consistent with those during the active time intervals (see column density of state with rate lower than 0.4 c s^{-1} and A_2 state). This behavior suggests that the $N_{\rm H}$ values in the low emission levels could be an indication of the matter distribution along the orbit, while additional mechanisms come into play during flaring activity.

The iron fluorescence lines show an interesting evolution: the centroid is at ∼6.8 keV when the source is in the JKL state while it shifts up to ∼7.1 keV at higher fluxes. As the iron line centroid is correlated with 2–10 keV unabsorbed flux (see Tables 1 and 2), line emissions at ∼6.8 and ∼7.1 keV could come from highly ionized iron ions: the ionization level is higher than Fe_{XXV} and Fe_{XX} for the states A_2 and JKL, respectively (Kallman et al. 2010). Since the theory predicts that the iron line intensity ratio I_{K_β}/I_{K_α} is ∼0.13 ph cm^{-2} s^{-1} (Kallman et al. 2010), the lack of a strong iron line at 6.4 keV during time intervals A_2 and JKL exclude that the observed iron line at ∼6.8–7.1 keV can be the fluorescence iron line K_β, not respecting this iron line intensity ratio. This behavior suggests that the X-ray flux produced by accretion onto the neutron star partly ionized the clump matter.

The limited statistics of our IGR J16328-4726 *XMM-Newton* data prevent us from studying the expected linear correlations between the continuum flux and the iron line flux or between the Fe equivalent width and the continuum parameters ($N_{\rm H}$ and luminosity), as reported by Giménez-García et al. (2015) and Torrejon et al. (2010).

This work has shown a complex picture that is compatible with accretion from an inhomogeneus wind (in't Zand 2005; Walter & Zurita Heras 2007). The transient emission produced by the accretion of matter from the companion wind indicates change in the wind density and temperature, not clearly correlated with the orbital phase. The inhomogeneities in the accreting material are able to give a physical interpretation of the short flares observed in both the *XMM-Newton* data and the previous *BeppoSAX* ones (Fiocchi et al. 2013).

Conversely, the clumpy wind model alone is not able to explain the few days of long flares observed with *INTEGRAL* from this source (Fiocchi et al. 2010). This evidence confirms that additional mechanisms are needed to explain the extreme variability seen in SFXT (Lutovinov et al. 2013; Bozzo et al. 2014).

The two proposed additional mechanisms of inhomogeneus wind are the quasi-spherical accretion model (Shakura et al. 2012, 2014) or the centrifugal and/or magnetic gating accretion (Bozzo et al. 2008, 2016). At this stage, for IGR J16328-4726, both mechanisms cannot be ruled out.

1. The theory of wind accretion in HMXB hosting a magnetic neutron star with transitions driven by centrifugal and magnetic barrier (Bozzo et al. 2008, 2016) requires a high magnetic field to explain the observed dynamic range (greater than $\sim 10^{14}$ G); unfortunately, the magnetic field in IGR J16328-4726 is unknown.
2. The quasi-spherical accretion model (Shakura et al. 2012, 2014) concerns the accretion onto slowly rotating X-ray pulsars: the spin period of IGR J16328-4726 is unknown. Furthermore, this theory predicts two regimes of accretion at the critical X-ray luminosity value of $\sim 4 \times 10^{36}$ erg s^{-1}. The present *XMM-Newton* data and the previous *Swift*/XRT results (Romano et al. 2013) allowed to extend the studied luminosity range, spanning from $\sim 6 \times 10^{33}$ to $\sim 3 \times 10^{36}$ erg s^{-1}. Unfortunately, the investigated luminosity values are always lower than the critical value preventing to study of X-ray behavior at very high luminosity.

Finally, we note that the accretion radius and the magnetospheric radius are highly sensitive to variations in the wind velocity and this wind velocity can significantly drop or be completely halted close to the neutron star when the matter is ionized (Ducci et al. 2010; Krticka et al. 2015), making the comparison data-model complicated.

The authors acknowledge the ASI financial support via ASI/INAF grants 2013-025-R.0 and the grant from PRIN/INAF 2014, toward a unified picture of accretion in High Mass X-Ray Binaries (PI: Sidoli).

We thank Dr. L. Sidoli for suggestions and discussion, which improved our work.

We thank the *XMM-Newton* duty scientists and science planners for making these observations possible.

REFERENCES

Baumgartner, W. H., Tueller, J., Markwardt, C. B., et al. 2013, ApJS, 207, 19
Bird, A. J., Malizia, A., Bazzano, A., et al. 2007, ApJS, 170, 175
Bodaghee, A., Courvoisier, T. J.-L., Rodriguez, J., et al. 2007, A&A, 467, 585
Bozzo, E., Falanga, M., & Stella, L. 2008, ApJ, 683, 1031
Bozzo, E., Oskinova, L., Feldmeier, A., & Falanga, M. 2016, A&A, 589, 102
Bozzo, E., Pavan, L., Ferrigno, C., et al. 2012, A&A, 544, 118
Bozzo, E., Romano, P., Ducci, L., Bernardini, F., & Falanga, M. 2014, in Proc. of ESA Conf., 10th Integral Workshop: A Synergistic View of the High-Energy Sky (Paris: ESA)
Bozzo, E., Romano, P., Ducci, L., et al. 2015, AdSpR, 55, 1255
Coleiro, A., Chaty, S., Zurita Heras, J. A., et al. 2013, A&A, 560, 108
Corbet, R. H. D., Barthelmy, S. D., Baumgartner, W. H., et al. 2010, ATel, 2588
Courvoisier, T. J.-L., Walter, R., Beckmann, V., et al. 2003, A&A, 411, L53
Ducci, L., Sidoli, L., & Paizis, A. 2010, MNRAS, 408, 1540
Federici, M., Martino, B. L., & Natalucci, L. 2009, in Proc. Conf. The Extreme Sky: Sampling the Universe above 10 keV (Trieste: PoS), 92
Fiocchi, M., Bazzano, A., Bird, A. J., et al. 2013, ApJ, 762, 19
Fiocchi, M., Sguera, V., Bazzano, A., et al. 2010, ApJ, 725, 68
Giménez-García, A., Torrejón, J. M., Eikmann, W., et al. 2015, A&A, 576, 108
Grupe, D., et al. 2009, ATel, 2075
in't Zand, J. J. M. 2005, A&A, 441, 1L
Jansen, F., Lumb, D., Altieri, B., et al. 2001, A&A, 365, 1
Kallman, T. R. 2010, SSRv, 157, 177
Kallman, T. R., palmeri, P., Bautista, M. A., et al. 2004, ApJS, 155, 675
Krticka, J., Kubat, J., & Krtickova, I. 2015, A&A, 579, 111
Lutovinov, A. A., Revnivtsev, M. G., Tsygankov, S. S., & Krivonos, R. A. 2013, MNRAS, 431, 327
Persi, P., Fiocchi, M., Tapia, M., et al. 2015, AJ, 150, 21
Romano, P., Ducci, L., Mangano, V., et al. 2014, A&A, 568, 55
Romano, P., La Parola, V., Vercellone, S., et al. 2011, MNRAS, 410, 1825
Romano, P., Mangano, V., Ducci, L., et al. 2013, AdSpR, 52, 1593
Shakura, N., Postnov, K., Kochetkova, A., et al. 2012, MNRAS, 420, 216
Shakura, N., Postnov, K., Sidoli, L., et al. 2014, MNRAS, 442, 2325
Sidoli, L. 2011, PoS, accepted (arXiv:1111.5747)
Torrejon, J. M., Schulz, N. S., Nowak, M. A., & Kallman, T. R. 2010, ApJ, 715, 947
Ubertini, P., Lebrun, F., Di Cocco, G., et al. 2003, A&A, 411, L131
Walter, R., Lutovinov, A. A., Bozzo, E., & Tsygankov, S. S. 2015, A&A, 23, 2
Walter, R., & Zurita Heras, J. 2007, A&A, 476, 335
Wilms, J., Allen, A., & McCray, R. 2000, ApJ, 542, 914
Winkler, C., Gehrels, N., Schönfelder, V., et al. 2003, A&A, 411, 349